Opposing effects of impurity ion Sr^{2+} on the heterogeneous nucleation and growth of barite ($BaSO_4$)

Ke Yuan[1*], Vitalii Starchenko[1], Nikhil Rampal[1,2], Fengchang Yang[1], Xiaogang Yang[3], Xianghui Xiao[4], Wah-Keat Lee[4], Andrew G. Stack[1*]

[1]Chemical Sciences Division, Oak Ridge National Laboratory, Oak Ridge, TN 37831
[2]Department of Chemical Engineering, Columbia University, NY 10027
[3]FS-PETRA, Deutsches Elektronen-Synchrotron DESY, Notkestraße 85, D-22607 Hamburg, Germany
[4]National Synchrotron Light Source-II, Brookhaven National Laboratory, Upton, NY 11973
*Corresponding authors: Ke Yuan, yuank@ornl.gov; Andrew G. Stack, stackag@ornl.gov

Abstract

Nucleation of barite ($BaSO_4$) has broad implications in the geological, environmental and materials sciences. While impurity metals are common, our understanding of how they impact nucleation remains dim. Here, we used classical optical microscopy compared to fast X-ray nanotomography (XnT) to investigate heterogeneous nucleation of barite on silica *in situ* with Sr^{2+} as an impurity ion. The observed barite nucleation rates were consistent with classical nucleation theory (CNT), where barite crystals displayed a nonuniform size distribution exhibiting distinct morphologies and incubation periods in Sr free solutions. While undetectable with optical microscopy, nanotomography revealed that addition of Sr^{2+} enhances nucleation rates driven by the pre-factor in CNT, likely because both adsorbed Ba^{2+} and Sr^{2+} act as precursor sites on which nucleation occurs. Sr^{2+} simultaneously inhibits growth, however, leading to a homogeneous distribution of smaller crystals. This finding will enable an improved predictive understanding of nucleation in natural and synthetic environments.

Introduction

Nucleation and growth of crystals at solid-water interfaces are key processes in ore/mineral deposition, heavy metal sequestration, and materials synthesis[1, 2]. For example, the sparingly soluble mineral barite ($BaSO_4$) is formed from aqueous barium (Ba^{2+}) and sulfate (SO_4^{2-}) ions, which are relatively abundant and widely distributed in the near subsurface. It commonly forms as scale during oil and gas operations[3], and in materials science, barite is used as an additive in lead acid batteries that facilitates lead sulfate nucleation during discharge[4]. In environmental science, crystallization of barite can incorporate impurity metal contaminants, such as Ra^{2+} and Sr^{2+}, due to their chemical similarity with barium[5, 6]. Because of this, dissolution of Ra-bearing barite found in uranium mines is the critical factor controlling Ra^{2+} mobility[7]. Similarly, barite found in seawater that is undersaturated with respect to that phase is intimately linked to the presence of Sr^{2+} (i.e., "barite paradox"), where the Sr isotopes in barite could be a useful indicator for paleo-ocean environments[8]. It is known that impurities such as Sr^{2+} poison the advance of monomolecular steps observed on calcite and barite crystals under atomic force microscopy[9-12]. Barite forms solid solutions with the end member celestite ($SrSO_4$), and previous studies have resulted in a theory that strives to account for nucleation of ideal $Ba_xSr_{(1-x)}SO_4$ solid solutions[13-15]. However, theoretical predictions such as these on ideal systems have not been sufficiently validated by experimental results. For example, surface processes are known to play a central role in barite precipitation, such as barite formed on organic surfaces of living organisms and in confined pores[16, 17]. Despite its importance, the mechanisms by which the common impurity ion, Sr^{2+}, impacts interfacial processes leading to the heterogenous nucleation and growth of barite remain poorly understood.

There has been increasing evidence that nucleation of carbonates, phosphates, and iron oxides can occur via non-classical nucleation pathways, where crystals are not nucleated by individual ion attachment but form through a multistep reaction process with the presence of intermediate metastable phases and/or particle aggregation (e.g., dense liquid phases, prenucleation clusters, and polymorphs)[1, 2]. However, nucleation of other minerals (e.g., barite) under certain saturation states can be explained by the classical nucleation theory (CNT) and even each individual step in a multiple-step non-classical nucleation can be treated with CNT successfully[18]. Unlike calcite, which has multiple crystalline polymorphs and may contain several intermediate phases, barite has

no known polymorphs. This suggests its nucleation pathway(s) might be more limited than that of calcite. However, recent studies suggesting amorphous barite formation, raise new questions on whether barite nucleation follows CNT or not[19-21].

We focus on the heterogeneous nucleation and growth of barite at silica-water interfaces, where the influence of Sr^{2+} on both nucleation and growth of barite was investigated. Numerous methods, including optical/electron microscopy, atomic force microscopy, and X-ray scattering, have been developed to study crystal nucleation[22-26]. Optical microscopy has been routinely used in crystal nucleation studies by recording the number of crystals in a flow-cell[27]. Since nuclei need to grow into a large enough size in order to be resolved by the optical light, which often have a practical resolution close to one micrometer (ideal resolution from 200 nm to 350 nm estimated as half the wavelength). Early-stage nucleation events and nuclei smaller than the resolution limit cannot be taken into account as nuclei are much smaller than the practical resolution. Liquid-cell transmission electron microscopy (TEM) images of crystal nucleation from the very beginning with a very high resolution, but limited field of view and changes to chemistry due to the creation of radical species by the beam is a potential problem. Similar to TEM, the limited field of view of atomic force microscopy cannot yield sufficient crystal count statistics to analyze the density of nuclei on a substrate robustly[28, 29]. Small angle X-ray scattering (SAXS) and Grazing Incidence SAXS (GISAXS) are increasingly used methods (operating in the reciprocal space) to obtain total scattering volume and particle sizes. Particles size commonly observed in (GI)SAXS is between 1 and 50 nm, but once crystal growth into micron size ranges, they will not be "seen" by the X-ray beam in the small angle range[30-32]. While this valuable technique has expanded our understanding considerably, experiments are often limited in terms of the ranges of saturation index (SI) and/or nucleation density that can be explored and has the potential to underestimate nuclei density when large particles formed rapidly in the system. Furthermore, for GISAXS, quantification of the total number of nuclei relies on knowing the effective cross-sectional area of the beam on the substrate, which is often difficult to obtain accurately.

Here, we used a different approach, employing X-ray nanotomography (XnT) based on transmission X-ray microscope (TXM), to image the nucleation and growth of barite *in situ* with a field of view of 40 μm × 40 μm and a spatial resolution of 30 nm[33]. The fast XnT scan in less

than 1 minute provides sufficient temporal resolution to catch the rapid crystal growth process and to minimize radiation damages to the samples[34]. The 3D tomography provides the total number and mass of nuclei in the system, which yields the nucleation and growth rates, respectively. The tomography data also provides spatial distribution of crystals on the substrate, allowing growth rates from individual crystals of different orientations to be compared. Comparing XnT to conventional optical microscopy, we found that optical microscopy results provide reasonable estimates of the interfacial energy but underestimate the pre-factor term in CNT due to its poor resolution. By adding Sr^{2+}**,** we observe significant changes on the crystal morphology and a reduction in growth rate, but the nucleation rate is found to increase. In Sr-free solutions, a relatively higher growth rate is observed, but with a lower nucleation rate. In addition, crystals with a high-index crystal surface attach to the substrate appear earlier on the surface and develop into micron-sized crystals compared with barite attached via the (001) surface, which has longer incubation time and appear as small crystals. Tomography images were processed by using traditional and automated segmentation methods, developed based on a Convolutional Neural Network (CNN). Combined, we found Sr^{2+} suppresses barite growth while promoting nucleation, specifically, by increasing the pre-factor in CNT instead of the common attribution that are driven by a reduction in interfacial energy. The counteracting effect of Sr^{2+} on barite nucleation and growth may be relevant to the micron-sized Sr-bearing barite observed in marine sediments and could have general implications on the role of cation impurities played during nucleation and growth of other solid-solution minerals.

Methods

Solutions and flow cell systems

Solutions containing $BaCl_2$ (Sigma-Aldrich), $SrCl_2$(Sigma-Aldrich), and Na_2SO_4 (Sigma-Aldrich) were prepared by dissolving the salts into deionized water. The saturation index ($SI = \log([Ba^{2+}][SO_4^{2-}]/K_{sp,barite}$, $K_{sp,barite} = 10^{-9.98}$) of solutions used for barite nucleation is SI = 1.9, 2.1, and 2.5. Another set of Sr-rich solutions with Ba:Sr = 1:1 were prepared under similar SI with respect to pure barite (see supporting information, Table S1 for solution compositions). The flow cell consisted of two solution reservoirs in glass bottles containing the $BaCl_2$/$BaCl_2$ + $SrCl_2$ and Na_2SO_4 (whose concentrations were determined by the SI with respect to barite), a syringe pump set at flow rate of 100 μL/min (Cole Parmer, Model 270), a custom solution mixer, and a glass

capillary cell that served as a reaction vessel where nucleation was observed. The mixer is a sealed glass bottle of a maximum volume of 2.0 ml with two inlets from the stock solutions, and one outlet, whose lines were made of Teflon tubing (1/32" in inner diameter). Studies have shown that at SI > 2.0, homogeneous nucleation of barite may occur,[35, 36] but in other studies, homogeneous nucleation was not found at SI 2.1[37]. To minimize nucleation prior to the portion of the capillary that was imaged, the solution mixer was placed close to the inlet of the capillary, such that the volume of mixed solution prior to being exposed to the capillary about 0.5 mL and with a residence time of 2.5 min under flowing solution. We did not observe any signs of significant homogeneous nucleation during our experiments, which could lead to pressure increase in the mixer (indicated by an increase of solution volume) due to the homogeneously formed crystals blocking the outlet of tube. A magnetic stir bar inside the solution mixer mixed the solution by using a stir plate (Fisher Scientific, Model Lab Disc S55). The mixer and attached tubes were thoroughly cleaned in ultrasound water bath before each use. Square borosilicate tubes (500 μm × 500 μm inner diameter, VitroCom) were used for the optical microscopy measurements. Rounded quartz capillary tubes (100 μm to 150 μm inner diameter, Charles Supper Company) were used for the XnT. Glass tubes were soaked in piranha solutions overnight and washed by deionized water before use to remove any oils or films left from their manufacture. The thin capillaries carefully mounted onto a specially designed XnT cell where solution flowed from the bottom and drained simultaneously on the top without interrupting the stage rotation (Fig. S1, details on the flow cell will be reported separately). The thin capillaries were washed with 1 M HCl and deionized water after mounted on the XnT stage before flowing the growth solutions.

Optical microscopy

The heterogenous nucleation process of barite on the square glass tube was observed *in situ* by using an optical microscope (Olympus BX51) equipped with a digital camera and an image recording system. The field of view is 700 μm × 300 μm under a magnification of 300×. The image was taken every 5 minutes.

Fast X-ray nanotomography

XnT was performed with the TXM at the Full-field X-ray Imaging beamline (18-ID) of National Synchrotron Light Source II, Brookhaven National Laboratory. The TXM was operated at 9keV

and had a field of view of 40μm × 40μm and a resolution of 30 nm. The sample was imaged *in situ* in flow cell with an exposure time of 0.05 s for each projection and a total acquisition time of about 1 minute for a full 3D tomography scan. To minimize radiation artifacts, each XnT scan was followed by a 10 min rest during which no beam was exposed to the sample. Upon finishing the time-dependent nucleation studies at each SI, we performed three additional scans at a location upstream to the observed position in the flow direction (to avoid potential radical damage imposed by previous scans) in order to obtain experimental errors on the measured nuclei density (see supporting information, Error Analysis). The XnT data were processed and reconstructed in TomoPy[38-40]. Volume and surface area were calculated from the segmented images in Fiji ImageJ [41-43]. A surface resampling value within the Particle Analysis Toolbox in Fiji ImageJ[42] was used to reduce the noise and remove crystals below the resolution limit when counting the particle density (See Supporting Information for details). Volumes of the crystals were calculated based on the number of voxels within the segmented images, and masses of the precipitates was calculated based on barite density of 4.48 g/cm^3. In some cases, automatic segmentation of grayscale images was used where traditional thresholding method was challenging due to increasing noise in the dataset. Recently machine learning based image segmentation have been proved efficient in such challenging cases. In this work, we employed a Convolutional Neural Network (CNN) based segmentation method[44]. A small portion (1%) of the grayscale images and the corresponding manual segmentation images were used for training the network. The trained network was then applied to segment all the grayscale images.

Results

Nucleation kinetics of barite obtained by optical microscopy and XnT

We compared the barite nucleation kinetics obtained from optical microspecies and XnT under same solutions. Increasing number of crystals in Sr free (SI = 2.47) solutions were observed over time on both optical and XnT images (Fig. 1). Under optical light, larger crystals (>1 μm) exhibited a darker color compared to smaller ones (Fig. S2), and both were segmented as shown in the binary images (Fig. 1a). Average particle sizes range between 0.8 μm to 1.5 μm in optical microscopy, whereas average particle size is about 0.2 μm with fine resolution under XnT. At 175 min, significant numbers of crystals appeared to grow together as imaged by optical microscopy (Fig. 1a). The particle overlap became more significant at higher SI, where the nucleation density was

underestimated. It is reflected as the plateau on the counted nucleation density at 200 min in Fig 2a and 2b (highlighted by the boxes, data not used for fitting the nucleation rates). Significant growth was observed after 100 min in Sr free solutions under optical light, however, the 100 min apparent incubation time reduced to less than 25 min as revealed by XnT (Fig 2a, 2c). Nucleation density measured by optical microscopy is one order of magnitude lower than that measured by XnT (Fig. 2). With addition of Sr^{2+}, optical microscopy showed fewer crystals than in Sr-free solutions, whereas for XnT, more crystals were revealed in Sr-rich solutions. This is because in the presence of Sr^{2+}, a reduced particle size is observed. From the time dependency of the nucleation density the linear part of the curves can be used to obtain a slope as the nucleation rate. Nucleation rates were found to be 2 times higher on average when Sr^{2+} was added as revealed by XnT, whereas a contrary conclusion was obtained by optical light due to its low resolution in resolving small particles (Table 1).

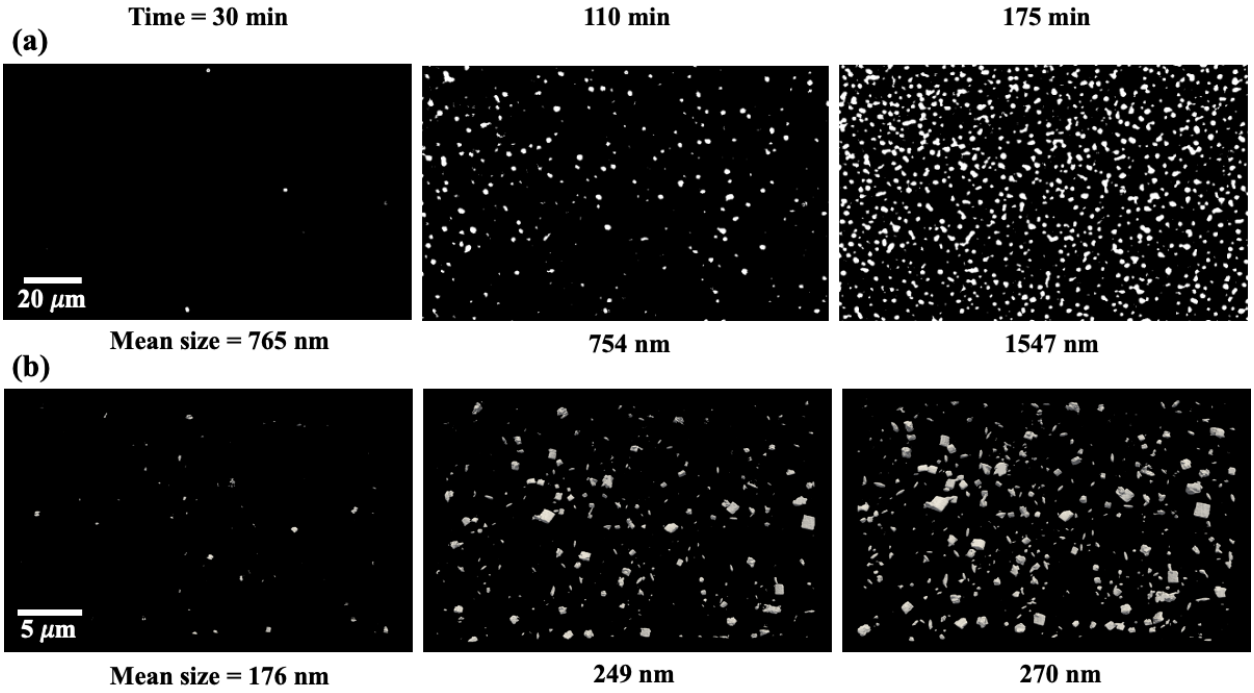

Figure 1. Images showing nucleation of barite in SI = 2.47, Sr-free solutions. (a) Optical microscopy. Binary images are shown to clearly illustrate the distribution and size of particles. (b) XnT at t = 30 min, 110 min, and 175 min. Notice the difference in the scale bar.

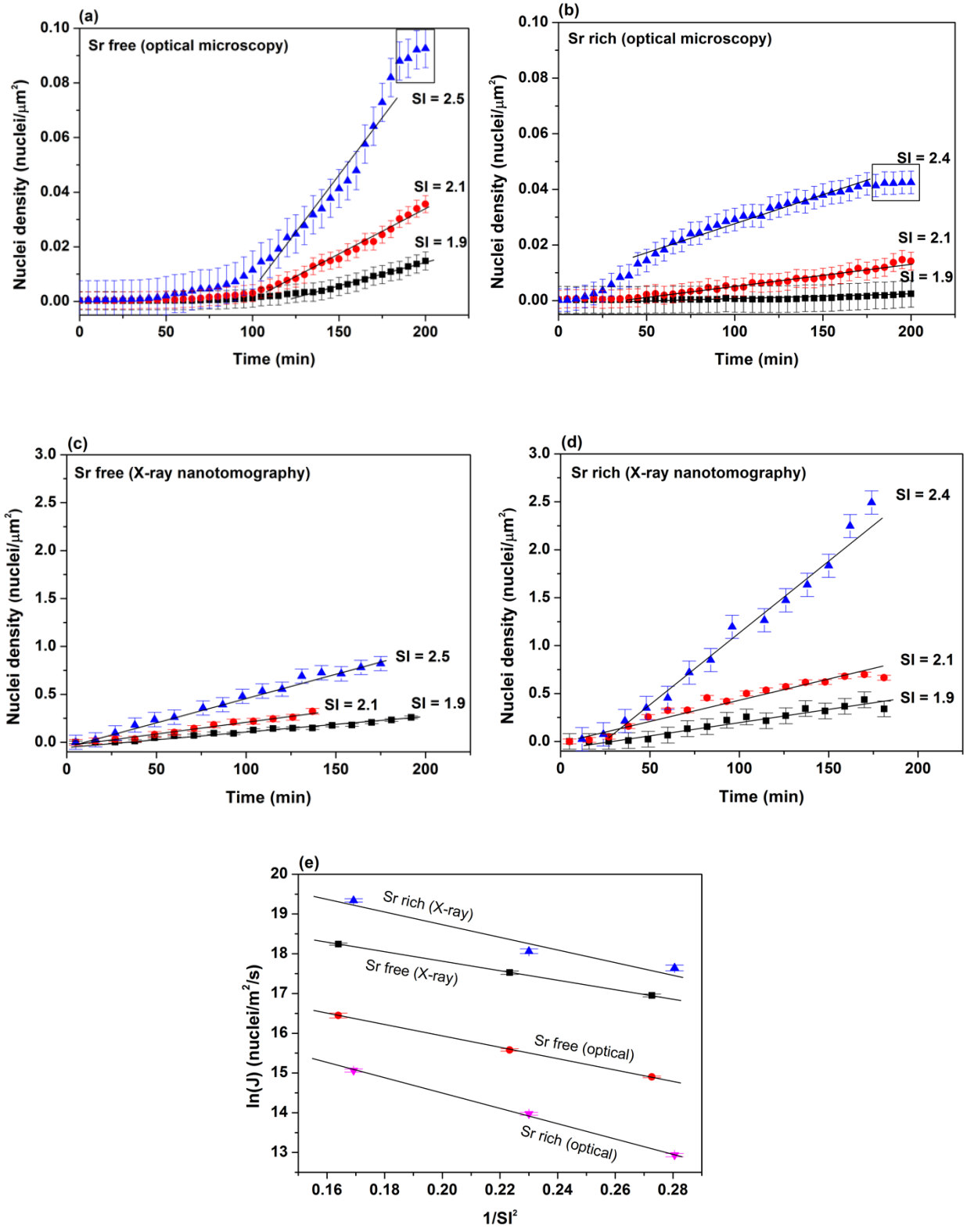

Figure 2. Nuclei density of barite changes with time in (a, c) Sr free and (b, d) Sr rich solutions of three different SI. Results obtained by (a, b) optical microscope was compared with that acquired

by (c, d) XnT. The areas indicated by the rectangle indicate where nuclei density measurements become unreliable using optical microscopy due to an inability to resolve individual particles. (e) ln(*J*) *vs.* 1/SI^2 plot for the calculations of pre-factor and interfacial energy in the classical nucleation theory.

Table 1. Nucleation rates of barite determined by using optical microscopy and XnT.

	Optical microscopy	**XnT**
SI (Sr free)	**Nucleation rate** $\times 10^6$ **(nuclei/m^2/s)**	**Nucleation rate** $\times 10^7$ **(nuclei/m^2/s)**
1.92	2.96 ± 0.06	2.30 ± 0.08
2.12	5.83 ± 0.19	4.08 ± 0.17
2.47	13.89 ± 0.79	8.37 ± 0.21
SI (Sr rich)	**Nucleation rate** $\times 10^6$ **(nuclei/m^2/s)**	**Nucleation rate** $\times 10^7$ **(nuclei/m^2/s)**
1.89	0.41 ± 0.02	4.60 ± 0.33
2.09	1.17 ± 0.04	7.00 ± 0.41
2.43	3.48 ± 0.15	25.10 ± 1.04

We used CNT originally derived for homogeneous nucleation to fit the data and it was plotted as ln(*J*) vs. 1/SI^2 in Fig. 2e. The fitted slope and intercept corresponding to interfacial energy and pre-factor, respectively, based on equation (1).

$$J = \Gamma exp\left(\frac{-\Delta G^*}{kT}\right)$$

$$\Delta G^* = \frac{B\sigma^3 V_{mol}^2}{(2.3SI \times kT)^2}$$

$$\ln J = \ln \Gamma + \left(\frac{-B\sigma^3 V_{mol}^2}{2.3^2 (kT)^3}\right) \times \frac{1}{SI^2} \qquad \text{Eq. 1}$$

Where *J* is the nucleation rate in nuclei/m^2/s, *B* is the geometric factor (16.76, treated as spherical particles in order to compare optical with XnT results), σ is the interfacial energy in J/m^2, V_{mol} is the molar volume of barite (52.11 cm^3/mol), SI is the saturation index of the solution, *k* is the Boltzmann constant, *T* is the temperature in K, Γ is the pre-factor term accounting for ion diffusion, desolvation, and other secondary processes at the solid-water interface.

Interfacial energies showed a slight increase by about 10% in Sr rich solutions as showed in results measured by both optical and X-ray microscopy (Table 2). Even though the absolute number of nuclei on the substrate may be underestimated by optical microscopy, the slope which represents

the gradient of nuclei density increase with time can still be fitted with reasonable accuracy by using optical microscopy (Fig. 2e). On the other hand, the pre-factor term (intercept of lines) is underestimated by the optical microscopy, in that the results obtained by X-ray microscopy yielded a higher pre-factor than that obtained by the optical microscopy (Table 2).

Table 2. Fitted pre-factor lnΓ and interfacial energy (σ) by optical microscopy (optical) and XnT (X-ray) for the heterogenous nucleation of barite.

Samples	**ln Γ (nuclei/m²/s)**	**σ (mJ/m²)**
Sr free (optical)	18.72 ± 0.01	34.53 ± 0.03
Sr rich (optical)	18.31 ± 0.05	38.23 ± 0.15
Sr free (X-ray)	20.19 ± 0.02	32.67 ± 0.09
Sr rich (X-ray)	22.08 ± 0.71	36.42 ± 2.48

Growth kinetics of barite crystals

Volume data obtained from segmented tomography images was used to calculate the volume of barite crystals. In order to obtain the growth rate of the crystals in the commonly used units of mol/m^2/s, here, two types of surface areas, substrate surface area and crystal surface area, were used. Crystal surface areas are the ideal measurement for computing the growth rate, but as we show, the substrate surface area is a more robust measurement, and the derived growth rate is less prone to uncertainty. Here, we demonstrated that these two methods of calculating the surface area provided different perspectives in understanding the barite growth kinetics. When the substrate surface area was used, which is the underneath area of the silica glass imaged by XnT, the growth rate increased with increasing SI in both Sr-free and Sr-rich solutions (Fig 3a and 3b). The fitted slopes in Fig. 3 indicated that the growth rates are similar in Sr-free and Sr-rich solutions of the same SI (Table 3.), that is, the fraction of barite on the substrate grows at a similar rate no matter if Sr^{2+} was added or not. However, when surface areas of the crystals were calculated, growth rates were reduced by about half in solutions with Sr^{2+} (Fig. 4 and Table 3). Crystal surface area was estimated by summing the geometric surface areas of all the individual crystals, which were calculated from the number of voxels occupied by barite, with an approximation that all crystals exhibited a cubic shape. The surface areas per gram of barite (specific surface areas) were higher in all Sr rich solutions, corresponding to a small particle size (Fig. 4a). The crystal surface area-

based growth rates do not show statistically significant variations with SI (Fig. 4b), which likely arises because the (significant) uncertainty introduced by estimating the geometric surface area is larger than the variation with SI. We also tried to directly calculate the crystal surface area from the tomography data using surface meshes enclosing all crystals. Both manually segmented data and machine-learning based automated segmentation results were compared (Fig. S3). This estimation has high uncertainty for small crystals due to challenges in creating reasonable surface mesh when the surface to mass ratios were high (Fig. S4 and Table S2). However, growth rates obtained by both geometric-based and directly calculated surface areas showed a reduction in Sr-rich solutions compared to that in Sr-free solutions.

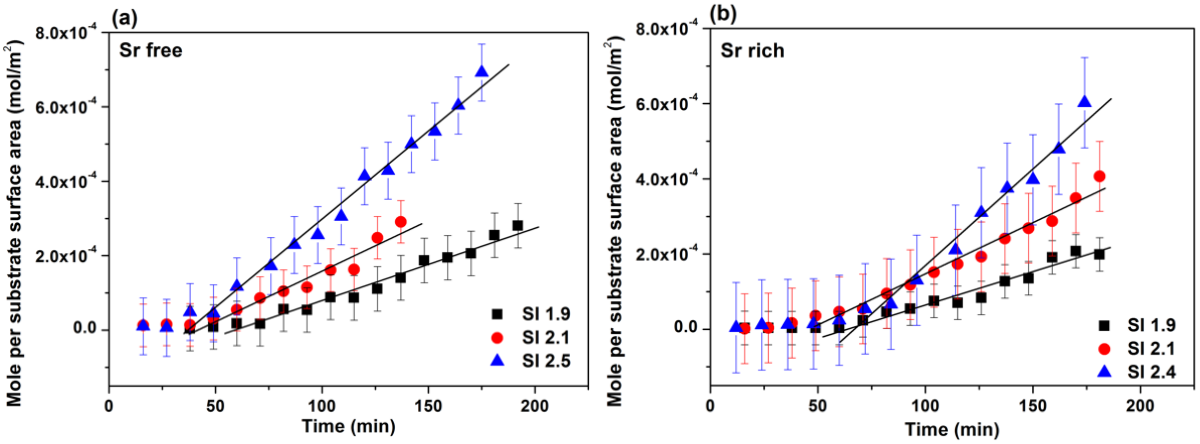

Figure 3. Substrate surface area-based growth rates of barite measured by XnT in (a) Sr-free and (b) Sr-rich solutions.

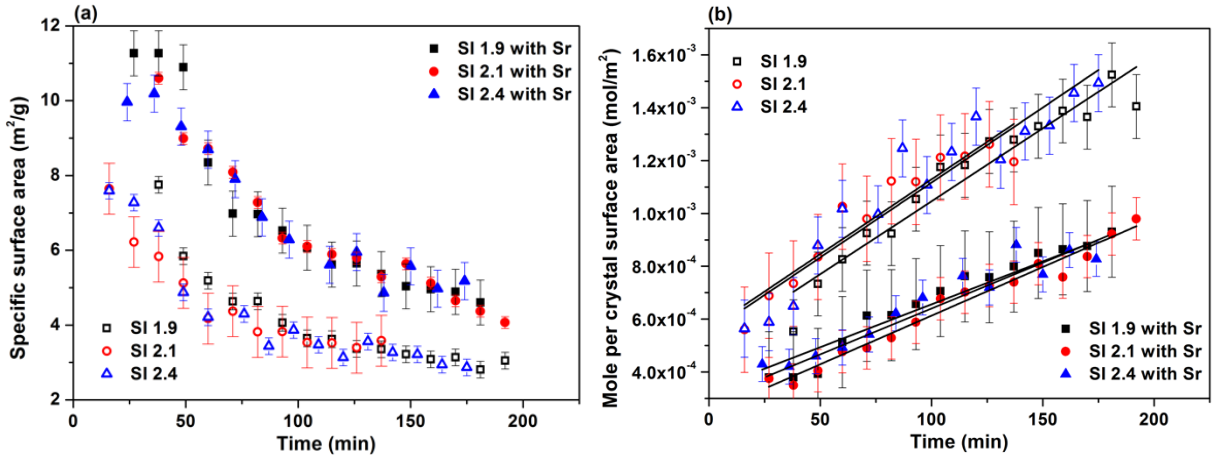

Figure 4. Changes of the crystals (a) specific surface areas and (b) Geometric crystal surface area-based growth rates calculated in Sr-free (hollow symbols) and Sr-rich solutions (solid symbols).

Table 3. Growth rates of barite determined by using XnT.

	Substrate surface area	Crystal surface area
SI (Sr free)	**Growth rate $\times 10^{-8}$ (mol/m^2/s)**	**Growth rate $\times 10^{-8}$ (mol/m^2/s)**
1.92	3.37 ± 0.17	9.21 ± 0.71
2.12	4.40 ± 0.35	9.44 ± 0.99
2.47	7.90 ± 0.30	9.46 ± 0.89
SI (Sr rich)	**Growth rate $\times 10^{-8}$ (mol/m^2/s)**	**Growth rate $\times 10^{-8}$ (mol/m^2/s)**
1.89	2.85 ± 0.20	5.90 ± 0.28
2.09	4.38 ± 0.22	6.13 ± 0.27
2.43	8.37 ± 0.48	5.41 ± 0.48

To fit our substrate surface area-based growth rate, we used a simplified linear rate law (equation 2) derived from transition state theory.

$$r = k\left(\frac{Q}{K_{sp}} - 1\right) \qquad \text{Eq. 2}$$

where r is the growth rate of barite in mol/m^2/s, K_{sp} is the solubility product of barite $= 10^{-9.98}$, Q is the ion activity product of $a_{Ba^{2+}} \cdot a_{SO_4^{2-}}$, k is the forward rate constant. From the ($Q/K_{sp} - 1$) vs. r plot, we obtained the rate constants in Sr-free and Sr-rich solutions from the slopes which showed the average value of 2.47 ± 0.50 $\times 10^{-10}$ mol/m^2/s. We also analyzed growth rates obtained by optical microscopy which were up to one order of magnitude higher at highest SI = 2.4 than that calculated by XnT (Fig. S5 and Table S3). We attribute this discrepancy to the defocused edges of crystals under optical light, which leads to an overestimation of the surface coverage of crystals on the substrate.

Homogenous crystal distributions in Sr-rich solutions

As mentioned previously, the nucleation density in Sr-rich solutions was underestimated using optical microscopy because the crystals were smaller than the practical resolution limit, while waiting for longer times led to an inability to resolve individual crystals (Fig. 2). In solutions of SI = 2.47 at t = 175 min, majority of the particles are between 100 nm to 200 nm in both Sr-free and Sr-rich solutions (Fig. 5). However, a significant number of large particles having sizes exceeding 400 nm were found in Sr-free solutions (Fig. 5a, 5c), but not in Sr-rich solutions (Fig. 5b, 5d). As showed before in Fig 3, adding Sr^{2+} did not change the substrate surface area-based estimate of the growth rate of barite, but changed how barite particles were distributed on the substrate. That is, in addition to being smaller due to a lower growth rate, they were more uniformly distributed. This

results in a narrower size distribution relative to the Sr-free case. A similar trend was observed in two other solutions at lower SI, whereas the effects from strontium became more obvious with increasing SI (Fig. S6).

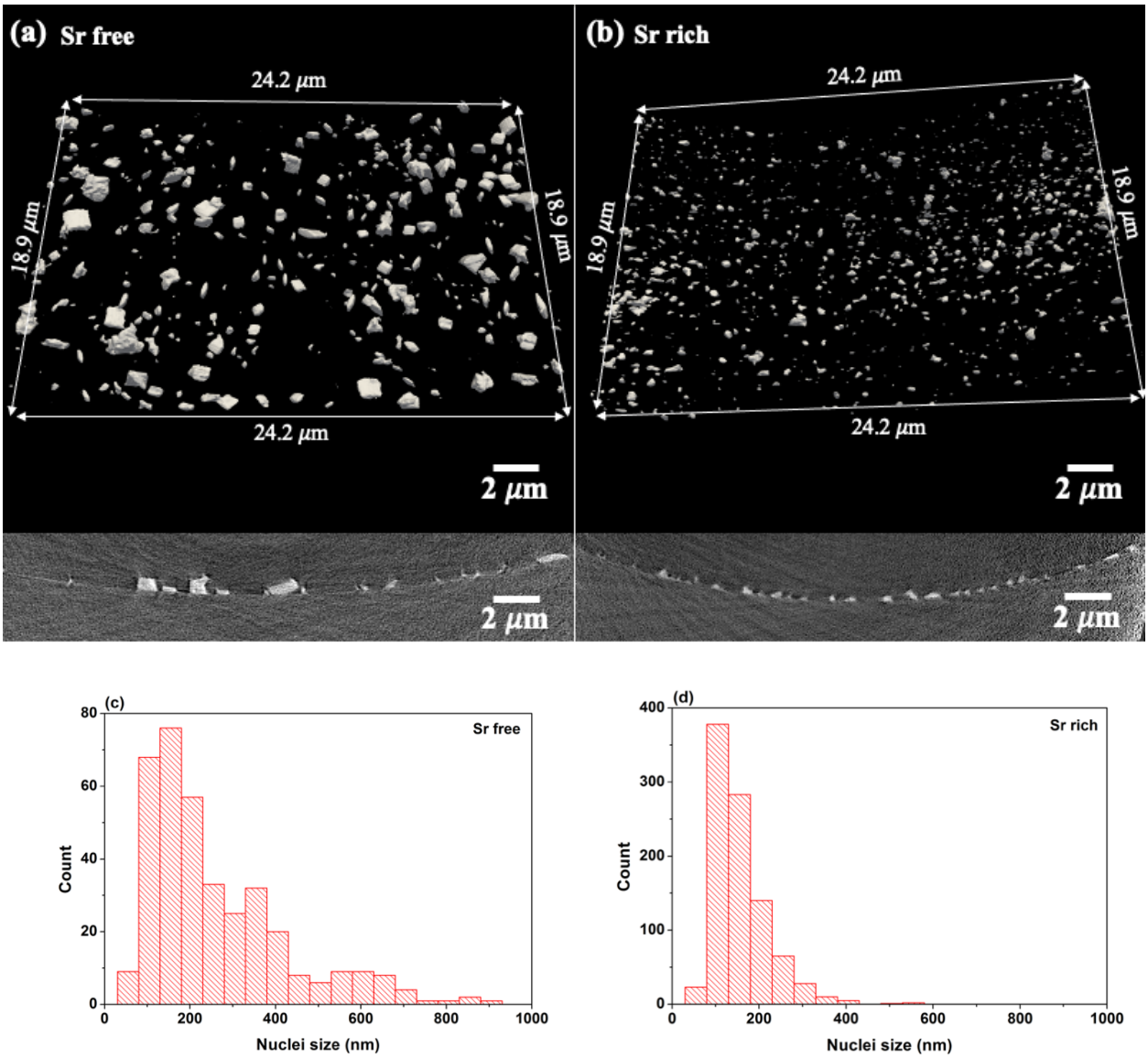

Figure 5. Three-dimensional view of barite crystal morphology in (a) Sr-free and (b) Sr-rich solutions with SI = 2.47 at 175 min. Cross-sectional views of the nanotomography data were shown below. Corresponding particle size distributions were shown in (c) and (d).

Orientation-dependent incubation time of barite crystals

Because crystals in Sr-free solutions at SI = 2.4 grow into large sizes with visible crystal facets, we isolated and aligned part of the data to show evolution of individual crystals with time (Fig 6.).

We tracked 6 crystals in total with crystals 1, 2, and 3 having a rhombic shape with a high-index surface attached to the substrate and their (210) and (100) surfaces are the major facets visible in Fig. 6. Crystals 4, 5, and 6 all have their (001) surface attached to the substrate instead, appearing as needle-like crystals. Interestingly, crystals 1, 2, and 3 had a short incubation time and appeared first on the substrate at times earlier than 49 min. All other crystals, including 4, 5, and 6, were observed at later times. All 6 crystals had a similar growth rate in the range of (6.49~11.8) $\times$ 10^{-8} mol/m^2/s (Fig. 6g), which is consistent with the global growth rate (9.46 $\times$ 10^{-8} mol/m^2/s) showed in Table 3.

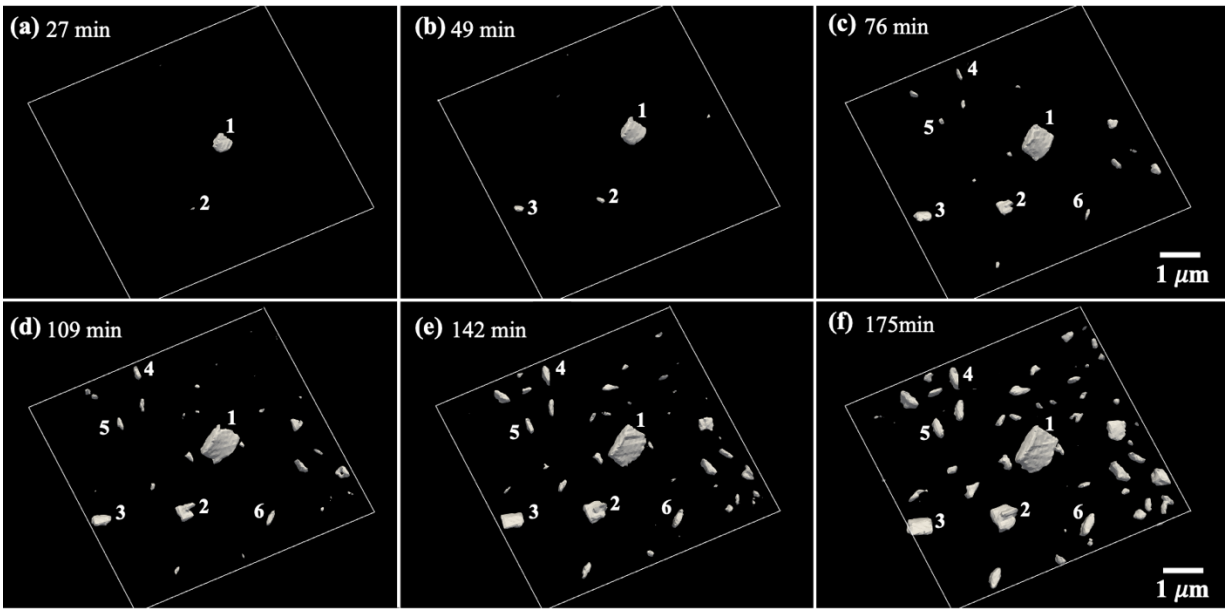

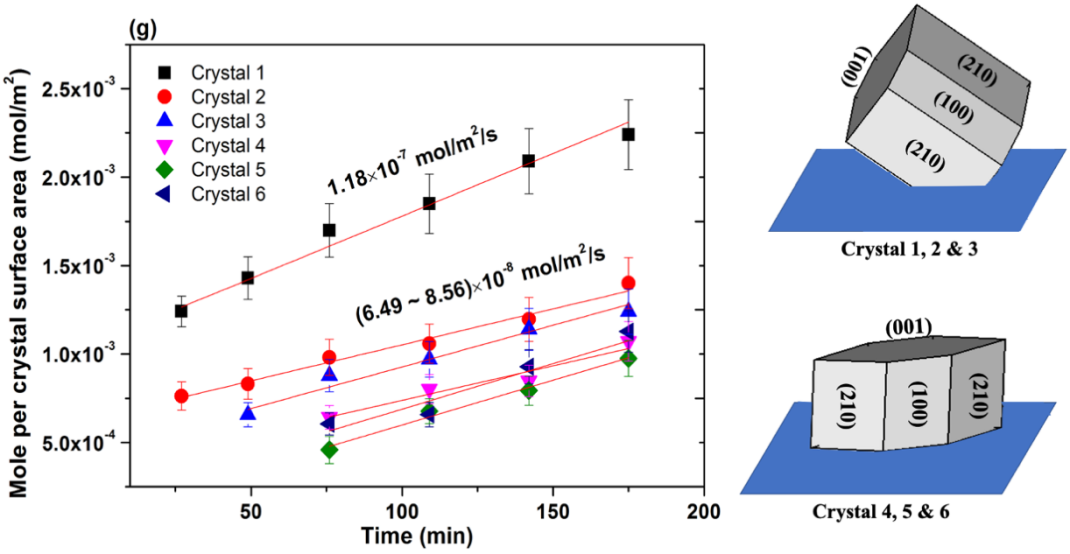

Figure 6. Zoomed-in view (7.1μm × 6.3 μm) of barite growth in Sr-free (SI = 2.43) solutions as a function of time (a-f). (g) Growth kinetics of 6 individual crystals as labeled in (a) to (f). Pictures on the left showed orientations of two types of barite crystals.

Effects of (Ba,Sr)SO_4 solid solution on nucleation kinetics

If the precipitates are not pure barite, but a mixed (Ba_x,Sr_{1-x})SO_4 solid solution phase, we need to consider the effects of the solid solution on the nucleation rate. Based on C.M. Pina 2001 et al[13], the composition (x) of the solid solution will impact the nucleation rate (J). The equation (1) can be rewritten as:

$$J(x) = \Gamma(x)\exp[\frac{-B\sigma^3(x)V_{mol}^2(x)}{k^3T^3(\ln S(x))^2}] \qquad \text{Eq. 3}$$

where S (supersaturation index), σ (interfacial energy), V_{mol}(molar volume) and Γ (pre-factor) are not constants but a function of composition (x) of the solid. These parameters all increase with the increase of x (Fig. S7).

The pre-factor Γ can be expressed in equation (4)[45]:

$$\Gamma(x) = \sqrt{\frac{\sigma(x)}{kT}}\left(\frac{kT}{hd_0^2}\right)\exp\left(\frac{-\Delta G_{diff}}{kT}\right) \qquad \text{Eq. 4}$$

where h is Plank's constant, and d_0 is the size of the nuclei (here we use d_0 = 1 nm as an approximation), ΔG_{diff} is the activation free energy for transferring a structural unit (ions) from the solution to the nucleus. Here, ΔG_{diff} was assumed to be constant and was back calculated

based on equation 3 and 4 using our measured nucleation rates in Sr-rich solutions with XnT (Table 1). The calculated ΔG_{diff} was 170 kJ/mol when precipitating a pure barite phase. To identify the effect of this energy difference on nucleation rates, we calculated the theoretical supersaturation of solid solutions and their nucleation rates J as a function of x (Fig. 7). The curves appeared in similar shapes with maximum nucleation rates at x = 0.8~0.9 which were about 1.2 to 1.3 times higher than that of pure barite (x = 1). Of note, the maximum nucleation rates (Fig. 7b) do not correspond to the highest supersaturation values (Fig. 7a). These calculations predict that precipitation of a slightly Sr-rich barite (x = 0.8~0.9 in $(Ba_x,Sr_{1-x})SO_4$) should have a higher nucleation rate than precipitating a pure barite phase.

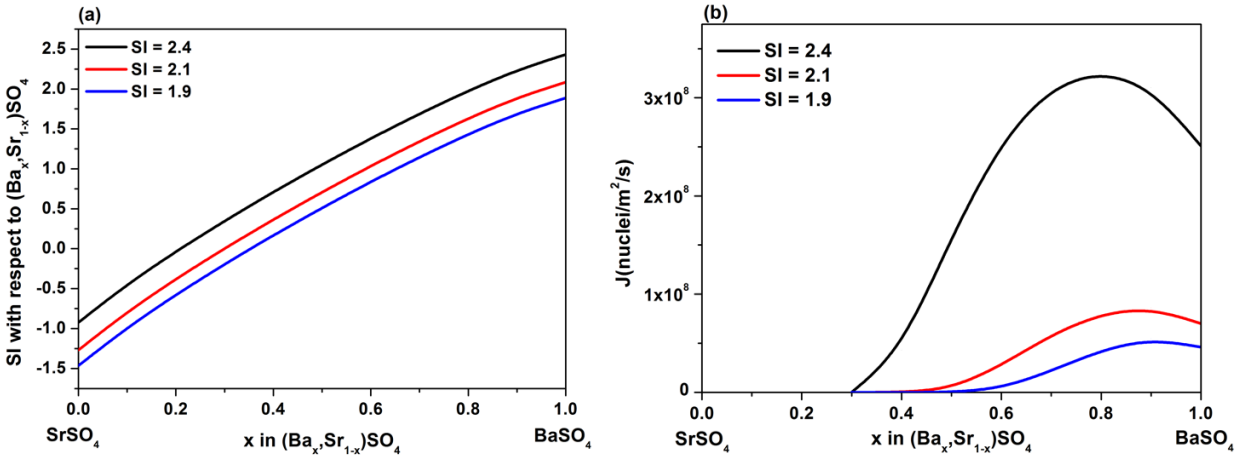

Figure 7. Calculated (a) supersaturation and (b) nucleation rates of $(Ba_x,Sr_{1-x})SO_4$ solid solutions at SI (with respect to pure barite) of 2.4, 2.1, and 1.9 in Sr-rich solutions.

Discussion

Sr^{2+} promoted barite nucleation

Previous studies have suggested that aqueous divalent ions may induce a higher nucleation rate of barite by lowering the surface free energy[46]. The interfacial energy of pristine barite in supersaturated solutions has been estimated to be about 76-105 mJ/m^2 during homogeneous nucleation[47]. Our results, however, indicate Sr^{2+} mainly enhances nucleation rates by increasing the kinetic pre-factor term (Γ), without lowering the effective interfacial energy of nucleation, 36.4 ± 2.5 mJ/m^2. (Table 1 shows the strontium slightly increases the interfacial energy, which would suppress the nucleation rate. See SI, Fig. S8.) The pre-factor is often poorly defined[2], which can be influenced by e.g., desolvation and diffusion of Ba^{2+} and SO_4^{2-} ions during nucleation, kinetic

limits on aggregation of smaller particles to a large cluster, or by efficiency of ion collisions with the mineral surface. The slope, related to interfacial energy, is well-characterized by both optical microscopy and X-ray tomography (Table 1), but often no changes are detected in the pre-factor with optical microscopy because of the limited resolution[27]. Thus, an effective interfacial energy is often fitted to the experimental nucleation data when applying CNT. Here, we showed that the pre-factor can be a critical term in explaining our observation, but it was resolvable only when high resolution XnT was applied.

When considering the effect of the strontium on the nucleation rate, it is important to first consider the formation of (Ba,Sr)SO_4 solid-solutions that will likely change the thermodynamics of precipitation. If solid solutions formed in our Sr-rich solutions of SI = 2.4, the predicted nucleation rate would be the highest when precipitating a ($Ba_{0.8}Sr_{0.2}$)SO_4 phase, where its nucleation rate is 1.3 times faster than forming a pure barite phase (Fig. 7). This prediction is rationalized by Nielson et al.[48], who observed a general inverse relation between solubility and surface energy among different crystals, where minerals with low solubilities tend to have higher surface energies in aqueous solution. Celestine is more soluble than barite[3], therefore, Sr-containing barite is more soluble and should have a low interfacial energy compared to pure barite. This reduction in interfacial energy favors the nucleation of a ($Ba_{0.8}Sr_{0.2}$)SO_4 phase over pure barite as predicted by the theory (Fig. 7). In contrast to the theory prediction, however, our measured nucleation rates in Sr-rich solutions are more than doubled (2.2 times higher on average) than that in Sr-free solutions (Table 1), instead of a 30% increase as expected by solid-solution effects. When (Ba,Sr)SO_4 solid solutions formed, the interfacial energy will decrease as predicted by theory (Fig. S7b). However, our data did not show a decrease in interfacial energies by adding Sr^{2+} (Table 1). Thus, even though nucleation of a slightly Sr-rich barite phase is likely more favorable thermodynamically, (Ba,Sr)SO_4 solid solution formation effects should result in a much smaller increase on nucleation rates in the Sr-rich solution than what is observed here.

To consider other possible ways that strontium may affect the nucleation of barite, we postulate that a likely initial step in the nucleation process that strongly influences the rate is the absorption of Ba^{2+} to a surface (Fig. 8)[31]. This is justified because our experiments were conducted in pH = 7 aqueous solutions where the silica surfaces are likely to be negatively charged[49, 50] and will

disfavor adsorption of negatively charged SO_4^{2-} ions. In the case where we have Ba^{2+}:Sr^{2+} = 1:1, the total number of divalent metal cations in the system is doubled, and if we assume that Ba^{2+} and Sr^{2+} have similar affinities for the silica surface, the total number of adsorbed cations on the silica surface likely increases. Previous studies have shown that hydration behavior of cations is the key mechanism governing their absorption on silicates and subsequent crystal growth in general[31, 51, 52]. Both Sr^{2+} and Ba^{2+} are divalent ions, and both Sr^{2+} and Ba^{2+} have similar large, exothermic hydration energies ($\Delta H_{hydration}$ = −1443 kJ/mol for Sr^{2+} and −1305 kJ/mol for Ba^{2+})[53]. Thus, it likely that Sr^{2+} and Ba^{2+} have similar affinities for silica surfaces, and indeed previous crystal truncation rod measurements indicate Sr^{2+} can form both inner- and outer-sphere complexes upon absorption to silicate minerals[54] and the adsorption Sr^{2+} and Ba^{2+} on silica have been found to have similar equilibrium constants for adsorption[55]. These relatively stable adsorbed Sr^{2+} species could provide structurally similar precursor sites for the subsequent absorption of SO_4^{2-} and/or other reactions leading to the formation of stable barite nuclei. A supporting argument for this interpretation is that the pre-factor, rather than the interfacial energy, was found to be responsible for the increased nucleation rates in the Sr-rich solutions relative to the Sr-free case. If the strontium were affecting the nucleation mechanism directly, one would expect a larger change in the interfacial free energy in the Sr-rich solution. What we envision is a multi-step nucleation process, whereby ions such as Sr^{2+} and Ba^{2+} first adsorb to silica surfaces, and subsequent nucleation processes occur by using these as precursor sites. Thus, the concentration of adsorbed species should be a variable in the CNT expression (Eq. 1), reflected here as changes in the pre-factor.

As a further note, previous work by Dai et al.[31] could not detect Ba^{2+} adsorption onto bare glass using a quartz crystal microbalance at SI = 1.1, while significant adsorption was found on organic-modified surfaces coated with self-assembled monolayers (SAM). However, an increase in the amount of absorbed Ba^{2+} (or Sr^{2+})[31] on a SAM did not necessarily correlate with a higher nucleation rate of barite, indicating there are interfacial processes other than an initial cation adsorption that limit the rate of nucleation. Since in our case a higher nucleation rate is observed, it is likely that the effects of strontium on barite nucleation are also substrate dependent (silica *vs*. SAM). We speculate that the origin of this substrate dependence is because the mechanisms of nucleation change on a SAM relative to a silica surface. This is justified because nucleation rates

on SAMs have been observed to be orders of magnitude higher than that on the silica used here. This argument is supported by observations that the orientations of nuclei can change depending on the terminal moiety of a SAM[56].

Strontium-inhibited barite growth

Impurities are known to change growth rates, and growth habit of crystals[57-60]. Impurity ions adsorbed at surface sites, including monomolecular steps or kink sites on those steps, result in retardation of the step advance. Both adsorption of Sr^{2+} on barite and precipitation of a $(Ba,Sr)SO_4$ solid solution could decrease the growth rate. Weber et al[11] showed that barite growth rate decreased at the 1:1 aqueous Ba^{2+}:Sr^{2+} ratios used here. High resolution chemical imaging showed uniform incorporation of Sr on barite surface steps. X-ray reflectivity found Sr^{2+} can simultaneously incorporate and adsorb on barite (001) surface[61]. Formation of $(Ba,Sr)SO_4$ solid solutions of any composition could lower the SI and therefore, the growth rate (Fig. 7a). Even if Sr^{2+} did not incorporate into barite, inhibition of barite growth could be achieved by non-incorporating impurities effects through influencing compositions of growing surfaces[62]. Our substrate surface area-based growth rates are similar in both Sr-free and Sr-bearing solutions (Table 3), reflecting the same chemical potential that provides the free energy gain for crystal growth. Addition of Sr^{2+} inhibited barite growing into large particles, yielding more nuclei and higher crystal surface area, resulting in a reduction of crystal surface area-based growth rate (Fig. 8).

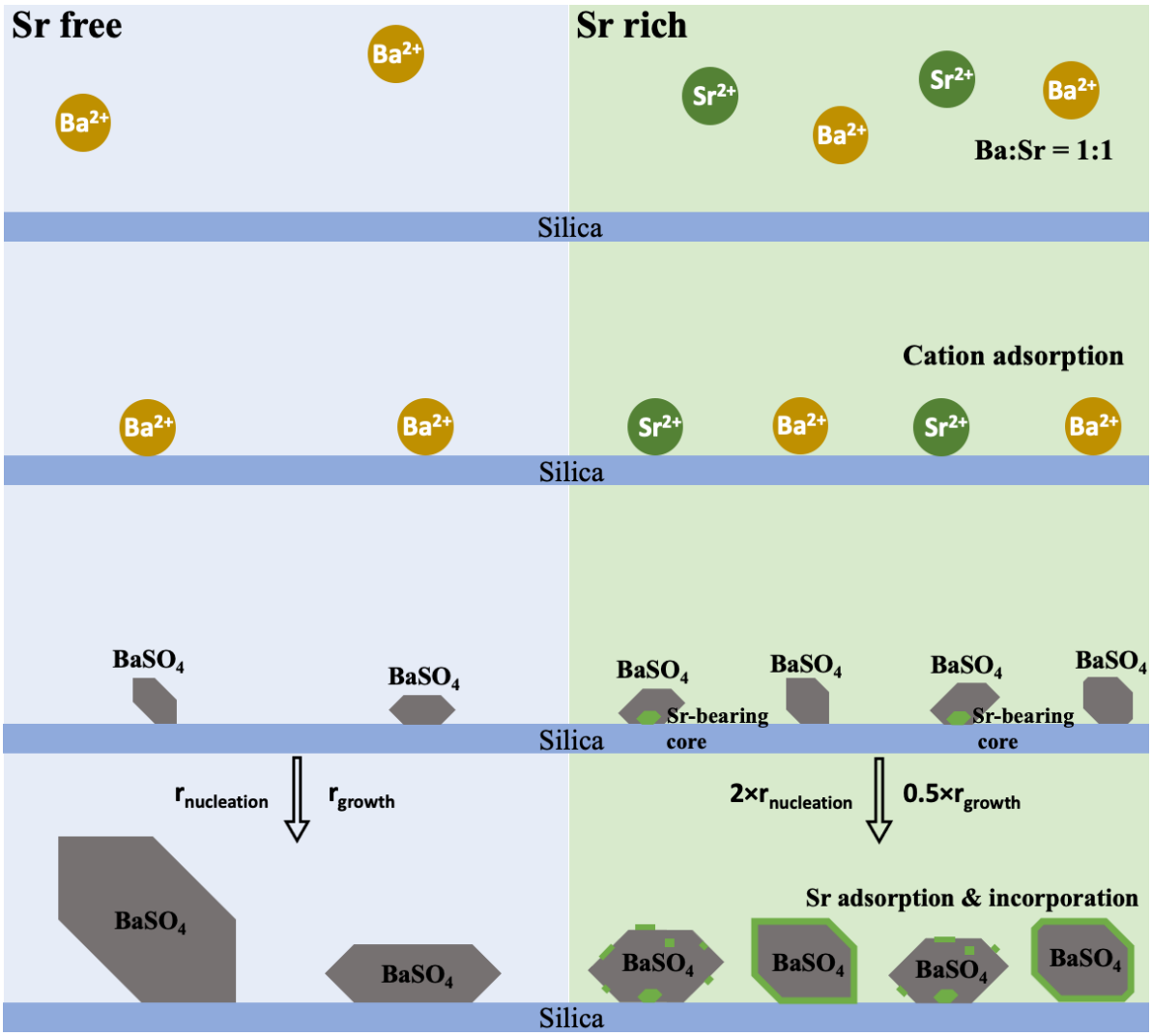

Figure 8. Mechanism of barite nucleation and growth without and with the influence of Sr^{2+}.

Conclusion

We investigated the role of Sr^{2+} in the heterogeneous nucleation of barite on silica surfaces and compared classical optical microscopy with advanced XnT. Optical microscopy failed to resolve small nuclei in the early stage resulting in a lower nucleation rate than the results obtained by XnT. Addition of Sr^{2+} was found to promote the nucleation rate by primarily increasing the kinetic pre-factor in CNT. To explain this, we suggest that adsorbed strontium species serve as precursor sites for nucleation in a similar capacity to adsorbed barium ions, but without changing the mechanism of nucleation. Crystals with different orientations exhibited different incubation times in Sr-free solutions. Crystals with their (001) surface attached appeared later on the substrate than crystals

attached by a high-index surface. The comparison of both imaging methods further improved our understanding on the nucleation and growth mechanism of barite and reflected a counter effect of impurity metals on the crystal nucleation and growth kinetics.

Acknowledgement

This work is supported by the U.S. Department of Energy, Office of Science, Office of Basic Energy Sciences, Chemical Sciences, Geosciences, and Biosciences Division. This research used resources at FXI beamline (18-ID) of the National Synchrotron Light Source-II, a U.S. Department of Energy (DOE) Office of Science User Facility operated for the DOE Office of Science by Brookhaven National Laboratory under Contract No. DE-SC0012704. This research was conducted, in part, using instrumentation within ORNL's Materials Characterization Core provided by UT-Battelle, LLC under Contract No. DE-AC05-00OR22725 with the U.S. Department of Energy. This research used resources of the Compute and Data Environment for Science (CADES) at the Oak Ridge National Laboratory, which is supported by the Office of Science of the U.S. Department of Energy under Contract No. DE-AC05-00OR22725.

Supporting Information

Solution chemistry; liquid XnT flow cell and error analysis; additional optical and nanotomography images; calculated parameters for solid solutions in CNT; growth rates obtained from optical images; growth rates calculated by using surface mesh areas; changes in pre-factor and interfacial energy to the calculated nucleation rates.

Reference

(1) De Yoreo, J. J.; Gilbert, P.; Sommerdijk, N.; Penn, R. L.; Whitelam, S.; Joester, D.; Zhang, H. Z.; Rimer, J. D.; Navrotsky, A.; Banfield, J. F.; Wallace, A. F.; Michel, F. M.; Meldrum, F. C.; Colfen, H.; Dove, P. M., Crystallization by particle attachment in synthetic, biogenic, and geologic environments. *Science* **2015,** 349, (6247).
(2) De Yoreo, J. J.; Vekilov, P. G., Principles of crystal nucleation and growth. In *Biomineralization*, Dove, P. M.; DeYoreo, J. J.; Weiner, S., Eds. 2003; Vol. 54, pp 57-93.
(3) Hanor, J. S., Barite-celestine geochemistry and environments of formation. In *Sulfate Minerals - Crystallography, Geochemistry and Environmental Significance*, Alpers, C. N.; Jambor, J. L., Eds. 2000; Vol. 40, pp 193-275.
(4) Boden, D. P., Selection of pre-blended expanders for optimum lead/acid battery performance. *J. Power Sources* **1998,** 73, (1), 89-92.
(5) Curti, E.; Fujiwara, K.; Iijima, K.; Tits, J.; Cuesta, C.; Kitamura, A.; Glaus, M. A.; Muller, W., Radium uptake during barite recrystallization at 23 ± 2 degrees C as a function of solution

composition: An experimental Ba-133 and Ra-226 tracer study. *Geochim. Cosmochim. Acta* **2010,** 74, (12), 3553-3570.
(6) Weber, J.; Barthel, J.; Klinkenberg, M.; Bosbach, D.; Kruth, M.; Brandt, F., Retention of Ra-226 by barite: The role of internal porosity. *Chem. Geol.* **2017,** 466, 722-732.
(7) Ouyang, B. J.; Akob, D. M.; Dunlap, D.; Renock, D., Microbially mediated barite dissolution in anoxic brines. *Appl. Geochem.* **2017,** 76, 51-59.
(8) McManus, J.; Berelson, W. M.; Klinkhammer, G. P.; Johnson, K. S.; Coale, K. H.; Anderson, R. F.; Kumar, N.; Burdige, D. J.; Hammond, D. E.; Brumsack, H. J.; McCorkle, D. C.; Rushdi, A., Geochemistry of barium in marine sediments: Implications for its use as a paleoproxy. *Geochim. Cosmochim. Acta* **1998,** 62, (21-22), 3453-3473.
(9) Wasylenki, L. E.; Dove, P. M.; Wilson, D. S.; De Yoreo, J. J., Nanoscale effects of strontium on calcite growth: An in situ AFM study in the absence of vital effects. *Geochim. Cosmochim. Acta* **2005,** 69, (12), 3017-3027.
(10) Bracco, J. N.; Grantham, M. C.; Stack, A. G., Calcite Growth Rates As a Function of Aqueous Calcium-to-Carbonate Ratio, Saturation Index, and Inhibitor Concentration: Insight into the Mechanism of Reaction and Poisoning by Strontium. *Cryst. Growth Des.* **2012,** 12, (7), 3540-3548.
(11) Weber, J.; Bracco, J. N.; Poplawsky, J. D.; Ievlev, A. V.; More, K. L.; Lorenz, M.; Bertagni, A. L.; Jindra, S. A.; Starchenko, V.; Higgins, S. R.; Stack, A. G., Unraveling the Effects of Strontium Incorporation on Barite Growth-In Situ and Ex Situ Observations Using Multiscale Chemical Imaging. *Cryst. Growth Des.* **2018,** 18, (9), 5521-5533.
(12) YuHang, C.; Asenjo, A.; Sanchez-Pastor, N.; Fernandez-Diaz, L.; Gomez, J.; Pina, C. M., Growth of $Ba_xSr_{1-x}SO4$ nano-steps on barite (001) face. *Surf. Sci.* **2007,** 601, (2), 381-389.
(13) Pina, C. M.; Putnis, A., The kinetics of nucleation of solid solutions from aqueous solutions: A new model for calculating non-equilibrium distribution coefficients. *Geochim. Cosmochim. Acta* **2002,** 66, (2), 185-192.
(14) Pina, C. M.; Enders, M.; Putnis, A., The composition of solid solutions crystallising from aqueous solutions: the influence of supersaturation and growth mechanisms. *Chemical Geology* **2000,** 168, (3-4), 195-210.
(15) Hunter, H. A.; Ling, F. T.; Peters, C. A., Metals Coprecipitation with Barite: Nano-XRF Observation of Enhanced Strontium Incorporation. *Environmental Engineering Science* **2020,** 37, (4), 235-245.
(16) Martinez-Ruiz, F.; Jroundi, F.; Paytan, A.; Guerra-Tschuschke, I.; Abad, M. D.; Gonzalez-Munoz, M. T., Barium bioaccumulation by bacterial biofilms and implications for Ba cycling and use of Ba proxies. *Nature Communications* **2018,** 9.
(17) Poonoosamy, J.; Curti, E.; Kosakowski, G.; Grolimund, D.; Van Loon, L. R.; Mader, U., Barite precipitation following celestite dissolution in a porous medium: A SEM/BSE and mu-XRD/XRF study. *Geochim. Cosmochim. Acta* **2016,** 182, 131-144.
(18) Smeets, P. J. M.; Finney, A. R.; Habraken, W.; Nudelman, F.; Friedrich, H.; Laven, J.; De Yoreo, J. J.; Rodger, P. M.; Sommerdijk, N., A classical view on nonclassical nucleation. *Proc. Natl. Acad. Sci. U.S.A.* **2017,** 114, (38), E7882-E7890.
(19) Ruiz-Agudo, C.; McDonogh, D.; Avaro, J. T.; Schupp, D. J.; Gebauer, D., Capturing an amorphous BaSO4 intermediate precursor to barite. *Crystengcomm* **2020,** 22, (8), 1310-1313.
(20) Martinez-Ruiz, F.; Paytam, A.; Gonzalez-Munoz, M. T.; Jroundi, F.; Abad, M. M.; Lam, P. J.; Bishop, J. K. B.; Horner, T. J.; Morton, P. L.; Kastner, M., Barite formation in the ocean: Origin of amorphous and crystalline precipitates. *Chem. Geol.* **2019,** 511, 441-451.

(21) Jones, F., Infrared investigation of barite and gypsum crystallization: Evidence for an amorphous to crystalline transition. *Crystengcomm* **2012,** 14, (24), 8374-8381.
(22) Hamm, L. M.; Giuffre, A. J.; Han, N.; Tao, J. H.; Wang, D. B.; De Yoreo, J. J.; Dove, P. M., Reconciling disparate views of template-directed nucleation through measurement of calcite nucleation kinetics and binding energies. *Proc. Natl. Acad. Sci. U.S.A.* **2014,** 111, (4), 1304-1309.
(23) Sleutel, M.; Lutsko, J.; Van Driessche, A. E. S.; Duran-Olivencia, M. A.; Maes, D., Observing classical nucleation theory at work by monitoring phase transitions with molecular precision. *Nature Communications* **2014,** 5.
(24) De Yoreo, J. J., In-situ liquid phase TEM observations of nucleation and growth processes. *Prog. Cryst. Growth Charact. Mater.* **2016,** 62, (2), 69-88.
(25) Stawski, T. M.; van Driessche, A. E. S.; Ossorio, M.; Rodriguez-Blanco, J. D.; Besselink, R.; Benning, L. G., Formation of calcium sulfate through the aggregation of sub-3 nanometre primary species. *Nature Communications* **2016,** 7.
(26) Li, Q. Y.; Jun, Y. S., Salinity-Induced Reduction of Interfacial Energies and Kinetic Factors during Calcium Carbonate Nucleation on Quartz. *J. Phys. Chem. C* **2019,** 123, (23), 14319-14326.
(27) Hu, Q.; Nielsen, M. H.; Freeman, C. L.; Hamm, L. M.; Tao, J.; Lee, J. R. I.; Han, T. Y. J.; Becker, U.; Harding, J. H.; Dove, P. M.; De Yoreo, J. J., The thermodynamics of calcite nucleation at organic interfaces: Classical vs. non-classical pathways. *Faraday Discuss.* **2012,** 159, 509-523.
(28) Smeets, P. J. M.; Cho, K. R.; Kempen, R. G. E.; Sommerdijk, N.; De Yoreo, J. J., Calcium carbonate nucleation driven by ion binding in a biomimetic matrix revealed by in situ electron microscopy. *Nature Materials* **2015,** 14, (4), 394-399.
(29) Nielsen, M. H.; Aloni, S.; De Yoreo, J. J., In situ TEM imaging of CaCO3 nucleation reveals coexistence of direct and indirect pathways. *Science* **2014,** 345, (6201), 1158-1162.
(30) Deng, N.; Stack, A. G.; Weber, J.; Cao, B.; De Yoreo, J. J.; Hu, Y. D., Organic-mineral interfacial chemistry drives heterogeneous nucleation of Sr-rich (Ba_x, Sr_{1-x})SO4 from undersaturated solution. *Proc. Natl. Acad. Sci. U. S. A.* **2019,** 116, (27), 13221-13226.
(31) Dai, C.; Stack, A. G.; Koish, A.; Fernandez-Martinez, A.; Lee, S. S.; Hu, Y. D., Heterogeneous Nucleation and Growth of Barium Sulfate at Organic-Water Interfaces: Interplay between Surface Hydrophobicity and Ba^{2+} Adsorption. *Langmuir* **2016,** 32, (21), 5277-5284.
(32) Fernandez-Martinez, A.; Hu, Y. D.; Lee, B.; Jun, Y. S.; Waychunas, G. A., In Situ Determination of Interfacial Energies between Heterogeneously Nucleated $CaCO_3$ and Quartz Substrates: Thermodynamics of CO_2 Mineral Trapping. *Environmental Science & Technology* **2013,** 47, (1), 102-109.
(33) Ge, M. Y.; Coburn, D. S.; Nazaretski, E.; Xu, W. H.; Gofron, K.; Xu, H. J.; Yin, Z. J.; Lee, W. K., One-minute nano-tomography using hard X-ray full-field transmission microscope. *Appl. Phys. Lett.* **2018,** 113, (8).
(34) Laanait, N.; Callagon, E. B. R.; Zhang, Z.; Sturchio, N. C.; Lee, S. S.; Fenter, P., X-ray-driven reaction front dynamics at calcite-water interfaces. *Science* **2015,** 349, (6254), 1330-1334.
(35) Roelands, C. P. M.; ter Horst, J. H.; Kramer, H. J. M.; Jansens, P. J., Analysis of nucleation rate measurements in precipitation processes. *Cryst. Growth Des.* **2006,** 6, (6), 1380-1392.
(36) Nielsen, A. E., *Kinetics of precipitation*. ed.; Pergamon: 1964; Vol. 18.
(37) Godinho, J. R. A.; Gerke, K. M.; Stack, A. G.; Lee, P. D., The dynamic nature of crystal growth in pores. *Scientific Reports* **2016,** 6.
(38) Gursoy, D.; De Carlo, F.; Xiao, X. H.; Jacobsen, C., TomoPy: a framework for the analysis of synchrotron tomographic data. *J. Synchrotron. Radiat.* **2014,** 21, 1188-1193.

(39) Pelt, D. M.; Gursoy, D.; Palenstijn, W. J.; Sijbers, J.; De Carlo, F.; Batenburg, K. J., Integration of TomoPy and the ASTRA toolbox for advanced processing and reconstruction of tomographic synchrotron data. *J. Synchrotron. Radiat.* **2016,** 23, 842-849.
(40) De Carlo, F.; Gursoy, D.; Marone, F.; Rivers, M.; Parkinson, D. Y.; Khan, F.; Schwarz, N.; Vine, D. J.; Vogt, S.; Gleber, S. C.; Narayanan, S.; Newville, M.; Lanzirotti, T.; Sun, Y.; Hong, Y. P.; Jacobsen, C., Scientific data exchange: a schema for HDF5-based storage of raw and analyzed data. *J. Synchrotron. Radiat.* **2014,** 21, 1224-1230.
(41) Schindelin, J.; Arganda-Carreras, I.; Frise, E.; Kaynig, V.; Longair, M.; Pietzsch, T.; Preibisch, S.; Rueden, C.; Saalfeld, S.; Schmid, B.; Tinevez, J.-Y.; White, D. J.; Hartenstein, V.; Eliceiri, K.; Tomancak, P.; Cardona, A., Fiji: An open-source platform for biological-image analysis. *Nature Methods* **2012,** 9, (7), 676-682.
(42) Doube, M.; Klosowski, M. M.; Arganda-Carreras, I.; Cordelieres, F. P.; Dougherty, R. P.; Jackson, J. S.; Schmid, B.; Hutchinson, J. R.; Shefelbine, S. J., BoneJ Free and extensible bone image analysis in ImageJ. *Bone* **2010,** 47, (6), 1076-1079.
(43) Schmid, B.; Schindelin, J.; Cardona, A.; Longair, M.; Heisenberg, M., A high-level 3D visualization API for Java and ImageJ. *Bmc Bioinformatics* **2010,** 11, 274.
(44) Kaira, C. S.; Yang, X. G.; De Andrade, V.; De Carlo, F.; Scullin, W.; Gursoy, D.; Chawla, N., Automated correlative segmentation of large Transmission X-ray Microscopy (TXM) tomograms using deep learning. *Mater. Charact.* **2018,** 142, 203-210.
(45) Schmelzer, J. W. P., On the determination of the kinetic pre-factor in classical nucleation theory. *J. Non-Cryst. Solids* **2010,** 356, (52-54), 2901-2907.
(46) Boon, M.; Jones, F., Barium Sulfate Crystallization from Synthetic Seawater. *Cryst. Growth Des.* **2016,** 16, (8), 4646-4657.
(47) Bosbach, D., Linking molecular-scale barite precipitation mechanisms with macroscopic crystal growth rates. *In: Water-Rock Interactions, Ore Deposits, and Environmental Geochemistry: A tribute to David A. Crerar. (R. Hellmann and S. A. Wood, eds.). The Geochemical Society* **2002,** 7, 97-110.
(48) Nielsen, A. E.; Sohnel, O., Interfacial tensions electrolyte crystal-aqueous solution, from nucleation data. *J. Cryst. Growth* **1971,** 11, (3), 233-242.
(49) Ong, S. W.; Zhao, X. L.; Eisenthal, K. B., Polarization of water-molecules at a charged interface - 2nd harmonic studies of the silica water interface. *Chem. Phys. Lett.* **1992,** 191, (3-4), 327-335.
(50) Sahai, N.; Sverjensky, D. A., Evaluation of internally consistent parameters for the triple-layer model by the systematic analysis of oxide surface titration data. *Geochim. Cosmochim. Acta* **1997,** 61, (14), 2801-2826.
(51) Kitamura, A.; Fujiwara, K.; Yamamoto, T.; Nishikawa, S.; Moriyama, H., Analysis of adsorption behavior of cations onto quartz surface by electrical double-layer model. *J. Nucl. Sci. Technol.* **1999,** 36, (12), 1167-1175.
(52) Stack, A. G.; Raiteri, P.; Gale, J. D., Accurate Rates of the Complex Mechanisms for Growth and Dissolution of Minerals Using a Combination of Rare-Event Theories. *J. Am. Chem. Soc.* **2012,** 134, (1), 11-14.
(53) Persson, I.; Sandstrom, M.; Yokoyama, H.; Chaudhry, M., Structure of the solvated strontium and barium ions in aqueous, dimethyl-sulfoxide and pyridine solution, and crystal-structure of strontium and barium hydroxide octahydrate. *Zeitschrift Fur Naturforschung Section a-a Journal of Physical Sciences* **1995,** 50, (1), 21-37.

(54) Lee, S. S.; Fenter, P.; Park, C.; Sturchio, N. C.; Nagy, K. L., Hydrated Cation Speciation at the Muscovite (001)-Water Interface. *Langmuir* **2010,** 26, (22), 16647-16651.
(55) Sverjensky, D. A., Prediction of the speciation of alkaline earths adsorbed on mineral surfaces in salt solutions. *Geochim. Cosmochim. Acta* **2006,** 70, (10), 2427-2453.
(56) Aizenberg, J., A bio-inspired approach to controlled crystallization at the nanoscale. *Bell Labs Technical Journal* **2005,** 10, (3), 129-141.
(57) Sangwal, K., Effect of impurities on the processes of crystal-growth. *J. Cryst. Growth* **1993,** 128, (1-4), 1236-1244.
(58) Sanchez-Pastor, N.; Pina, C. M.; Fernandez-Diaz, L., Relationships between crystal morphology and composition in the (Ba,Sr)SO_4-H_2O solid solution-aqueous solution system. *Chem. Geol.* **2006,** 225, (3-4), 266-277.
(59) Liang, Y.; Jacobson, A. J.; Rimer, J. D., Strontium Ions Function as Both an Accelerant and Structure-Directing Agent of Chabazite Crystallization. *Acs Materials Letters* **2021,** 3, (2), 187-192.
(60) Alamani, B. G.; Gale, J. D.; Rimer, J. D., Zinc Ions Modify Calcium Oxalate Growth by Distinct Transformation of Crystal Surface Termination. *Cryst. Growth Des.* **2021,** 21, (6), 3375-3383.
(61) Bracco, J. N.; Lee, S. S.; Stubbs, J. E.; Eng, P. J.; Jindra, S.; Warren, D. M.; Kommu, A.; Fenter, P.; Kubicki, J. D.; Stack, A. G., Simultaneous Adsorption and Incorporation of Sr2+ at the Barite (001)-Water Interface. *J. Phys. Chem. C* **2019,** 123, (2), 1194-1207.
(62) Pina, C. M., Inhibition of growth in solid solution-aqueous solution systems by non-incorporating impurities. *Surf. Sci.* **2011,** 605, (5-6), 545-550.

For Table of Contents Use Only

Opposing effects of impurity ion Sr^{2+} on the heterogeneous nucleation and growth of barite ($BaSO_4$)

Ke Yuan[1*], Vitalii Starchenko[1], Nikhil Rampal[1,2], Fengchang Yang[1], Xiaogang Yang[3], Xianghui Xiao[4], Wah-Keat Lee[4], Andrew G. Stack[1*]

Table of Contents Graphic

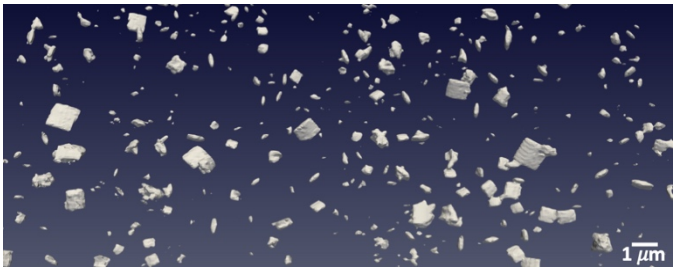

The nucleation and growth of barite crystals in solutions were imaged by using nanotomography under synchrotron X-ray beam. The results reflected a counter effect of impurity metals on the crystal nucleation and growth kinetics.